

Theory of moiré localized excitons in transition-metal dichalcogenide heterobilayers

David A. Ruiz-Tijerina,^{1,*} Isaac Soltero,² and Francisco Mireles¹

¹*Departamento de Física, Centro de Nanociencias y Nanotecnología,*

Universidad Nacional Autónoma de México. Apdo. postal 14, 22800, Ensenada, Baja California, México

²*Escuela Superior de Física y Matemáticas, Instituto Politécnico Nacional. Gustavo A. Madero, C.P. 07738, Ciudad de México, México*

(Dated: February 26, 2022)

Transition-metal dichalcogenide heterostructures exhibit moiré patterns that spatially modulate the electronic structure across the material's plane. For certain material pairs, this modulation acts as a potential landscape with deep, trigonally symmetric wells capable of localizing interlayer excitons, forming periodic arrays of quantum emitters. Here, we study these moiré localized exciton states and their optical properties. By numerically solving the two-body problem for an interacting electron-hole pair confined by a trigonal potential, we compute the localized exciton spectra for different pairs of materials. We derive optical selection rules for the different families of localized states, each belonging to one of the irreducible representations of the potential's symmetry group C_{3v} , and numerically estimate their polarization-resolved absorption spectra. We find that the optical response of localized moiré interlayer excitons is dominated by states belonging to the doubly-degenerate E irreducible representation. Our results provide new insights into the optical properties of artificially confined excitons in two-dimensional semiconductors.

I. INTRODUCTION

Atomically thin layers of semiconducting transition-metal dichalcogenides (TMDs) have emerged as a promising optoelectronics platform, based on their valley-dependent optical selection rules^{1–4} and enhanced optical activity mediated by strongly-bound excitons^{5,6}. Among these, so-called interlayer excitons (IXs) form in band-mismatched heterobilayers, where electrons and holes preferentially localize in different materials⁷ [Fig. 1(a)]. Being delocalized across the two crystals, IXs are especially susceptible to the heterostructure's stacking configuration. For instance, it has been shown that the IX energies can be tuned by means of the interlayer twist angle⁸, by their Stark shift in the presence of out-of-plane electric fields⁹, as well as hybridization with bright intralayer exciton states¹⁰. These and other examples^{11–13} suggest that manipulating IXs may constitute a viable way of tuning the optical properties of TMD-based heterostructures.

In closely aligned TMD heterobilayers, the slight incommensurability between the two lattices produces a moiré pattern¹⁴: an approximately periodic spatial modulation of the relative shift between the two materials. Due to the long-range periodicity of the moiré pattern, different regions of the heterostructure have an approximately commensurate stacking that determines the local value of the heterostructure's band gap¹⁵, and consequently the IX energy. Thus, the moiré pattern acts as an approximate superlattice potential for IXs, leading to zone folding and miniband formation^{16,17}, visible in experiments as a complex fine structure in the material's optical spectrum^{10,18–20}.

For certain material pairs, such as $\text{WSe}_2/\text{MoSe}_2$ and $\text{WSe}_2/\text{MoS}_2$, the moiré potential exhibits¹⁵ deep potential wells capable of localizing IXs^{21–23}, effectively forming tunable quantum emitter arrays with the periodicity of the moiré pattern. The optical response of such states is governed by their symmetry, inherited from that of the potential well and from the carrier Bloch functions at the localization center, giving rise to optical selection rules distinct from those of extended exciton states.

Here, we numerically study the localization and optical spectra of IX states confined by moiré potential wells in TMD heterobilayers. We focus on closely aligned, nearly commensurate structures, where the moiré supercell length is much larger than the exciton Bohr radius. This allows us to separate the exciton's center of mass (COM) and relative (RM) motions, and solve each problem individually by direct diagonalization methods to compute the low-energy exciton spectrum and wavefunctions. We report a sequence of localized exciton levels identified by their C_{3v} quantum numbers, which is robust for the different material pairs studied in this paper, based on *ab initio* parametrizations of their moiré potentials reported by Yu *et al.*¹⁵ We give detailed account of these states' optical selection rules for twisted heterobilayers close to parallel (R) and anti-parallel (H) stacking, and estimate the corresponding absorption spectra by considering the dominant processes mediated by hybridization with intralayer excitons²⁴. Our analysis reveals that the heterostructure's optical response is dominated by states with orbital wave functions belonging to the E irreducible representation of the group C_{3v} . Our results shed new light on the optical properties of IX states in 2D semiconductors confined by artificial potentials.

The rest of this paper is organized as follows: we discuss our theoretical model and its constraints in Sec. II. In Sections II A and II B we describe our numerical treatment of the IX relative-motion and center-of-mass problems, respectively, and present calculated spectra for moiré localized interlayer excitons in $\text{WSe}_2/\text{MoSe}_2$ and $\text{WSe}_2/\text{MoS}_2$ heterobilayers. The symmetry properties and optical selection rules of these states are discussed in Sec. III, and their numerical absorption spectra are presented in Sec. IV. Our concluding remarks appear in Sec. V.

II. MODEL

Our focus will be on semiconducting TMD heterobilayers with staggered band alignment, whose conduction- and valence-band edge states are localized in different layers. We

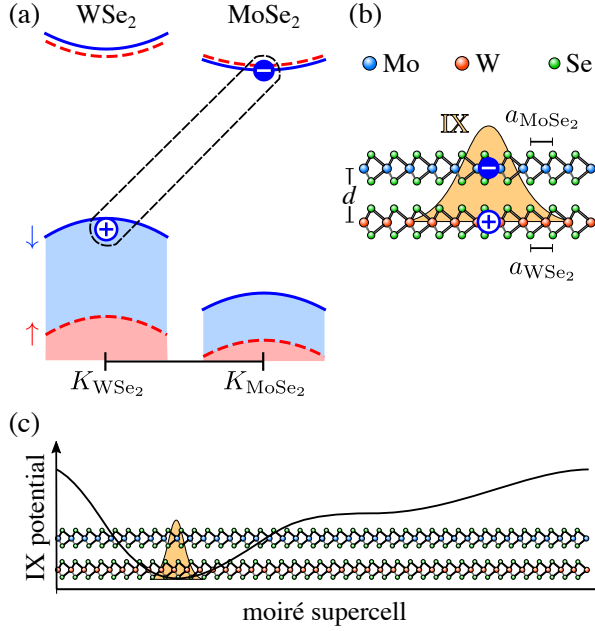


FIG. 1. (a) K -valley band alignment for the type-II heterobilayer WSe₂/MoSe₂. Blue solid (red dashed) curves represent spin-down (spin-up) electronic bands. An electron-hole pair excitation is also depicted, which binds into an IX. (b) Side view of the heterostructure, showing the spatial separation between the electron and hole forming the IX. The relative motion wavefunction is sketched in orange. (c) A broader side view of the heterostructure within a moiré supercell. The moiré potential is shown, with an IX localized at its minimum.

use the nomenclature MX₂/M'X'₂, where M'X'₂ (MX₂) is the TMD layer to which the bottom of the conduction band (top of the valence band) belongs, as sketched in Fig. 1(a). To describe interlayer excitons in the heterostructure, formed by an M'X'₂ electron of effective mass $m_{e'}$ and an MX₂ hole of effective mass m_h , we use the two-body Hamiltonian

$$H_{e-h} = \frac{p^2}{2M} + \frac{p^2}{2\mu} + U_K(|\mathbf{r}_e - \mathbf{r}_h|) + V_M(\mathbf{r}_e, \mathbf{r}_h). \quad (1)$$

Here, \mathbf{P} and \mathbf{p} represent the total and relative momenta;

$$M = m_{e'} + m_h, \quad \mu = \frac{m_{e'}m_h}{m_{e'} + m_h}, \quad (2)$$

are the total and reduced masses of the electron-hole system; U_K is the electrostatic interaction between the electron and hole at positions \mathbf{r}_e and \mathbf{r}_h ; and V_M represents the periodic moiré potential.

The system is assumed to be embedded in an environment with average dielectric constant ϵ , which together with the in-plane electric susceptibilities κ and κ' of the two layers defines the length scales (Table I) $r_* = 2\pi\kappa/\epsilon$ and $r'_* = 2\pi\kappa'/\epsilon$, below which electrostatic interactions in the corresponding TMD layer are screened. For simplicity, we adopt the long-range approximation defined by $\rho \equiv |\mathbf{r}_e - \mathbf{r}_h| \gg r_*, r'_*$, which gives the electron-hole interaction in the Keldysh form^{25,26}

$$U_K(\rho) = \frac{-e^2\pi}{2\epsilon r_{\text{eff}}} \left[H_0\left(\frac{\rho}{r_{\text{eff}}}\right) - Y_0\left(\frac{\rho}{r_{\text{eff}}}\right) \right], \quad (3)$$

where H_0 and Y_0 are a Struve function and a Bessel function of the second kind, respectively, and e is the elementary charge. The effective screening length $r_{\text{eff}} = r_* + r'_* + d$ accounts for the dielectric response of the additional layer, and in the case of IXs for the out-of-plane separation between their carriers, d [Fig. 1(b)]. For intralayer excitons in the heterostructure, the appropriate definition is $r_{\text{eff}} = r_* + r'_*$, whereas in a monolayer $r_{\text{eff}} = r_*$. As discussed in Ref. 25, this approximation overestimates the short-range interactions in the case of IXs, and the binding energies (Bohr radii) computed from (3) must be interpreted as an upper (lower) limit.

The moiré potential V_M varies over length scales of the order of the moiré superlattice constant [Fig. 1(c)]

$$a_M = \frac{a_{>}}{\sqrt{\delta^2 + \theta^2}}, \quad (4)$$

defined by the interlayer twist angle $\theta \ll 1$ and lattice mismatch $\delta = 1 - a_{<}/a_{>}$, where $a_{>}$ ($a_{<}$) is the larger (smaller) lattice constant of the two TMD layers. Based on Eq. (4) and the known lattice constants of the four main semiconductor TMDs (Table I), we estimate a_M for both R and H structures to be of order 10nm for heterobilayers with different chalcogens, and 100nm for those with matching chalcogens, like WSe₂/MoSe₂ and WS₂/MoS₂. By contrast, U_K binds electrons and holes into excitons with Bohr radii^{18,25,38} $a_B \approx 10$ -20 Å, over which V_M varies slowly. This allows us to treat the electron-hole pair as point-like, and located at the COM position \mathbf{R} . The moiré potential then becomes

$$V_M(\mathbf{r}_e, \mathbf{r}_h) \approx V_M(\mathbf{R}), \quad \mathbf{R} = \frac{m_e\mathbf{r}_e + m_h\mathbf{r}_h}{M}, \quad (5)$$

neglecting any RM dependence, and making the Hamiltonian (1) separable into a COM part and a RM part. This approach is especially well suited for studying excitons in WSe₂/MoSe₂ and WS₂/MoS₂ heterostructures with small twist angles, and less so in the case of strong misalignment

TABLE I. In-plane lattice constants a , effective electron and hole masses m_e and m_h , and screening lengths r_* (*in vacuo*) for the main semiconductor TMDs, extracted from the experimental and *ab initio* literature. We also show the (maximum) moiré superlattice parameters a_M for different heterobilayers, assuming perfect rotational alignment.

TMD	a [Å]	m_e/m_0	m_h/m_0	r_* [Å]	Heterostructure	d [Å]	a_M [nm]
MoS ₂	3.160 ^a	0.70 ^d	0.70 ^h	38.62 ⁱ	MoSe ₂ /MoS ₂	6.97 ^j	7.54
	3.140 ^b				MoSe ₂ /WS ₂	6.88 ^j	7.75
MoSe ₂	3.299 ^b	0.80 ^e	0.50 ^h	39.79 ⁱ	WSe ₂ /MoS ₂	6.83 ^j	8.05
	3.288 ^a				WSe ₂ /MoSe ₂	7.02 ^j	108.50
WS ₂	3.154 ^{a,c}	0.27 ^f	0.50 ^h	37.89 ⁱ	WSe ₂ /WS ₂	6.86 ^j	8.30
WSe ₂	3.286 ^a	0.50 ^g	0.45 ⁱ	45.11 ⁱ	WS ₂ /MoS ₂	6.76 ^j	248.70
	3.282 ^b						

^aReference [27], ^bReference [28], ^cReference [29], ^dReference [30],

^eReference [31], ^fReference [32], ^gReference [33], ^hReference [34],

ⁱReference [35], ^jReference [36], ^kReference [37]

angles and for heterobilayers formed with TMDs containing different chalcogens. In the following we shall focus on the former case, setting the twist angle to zero.

With (5), solutions to the Hamiltonian (1) have the form

$$\Psi(\mathbf{r}_e, \mathbf{r}_h) = F(\mathbf{R})f(\boldsymbol{\rho}), \quad (6)$$

where $\boldsymbol{\rho} \equiv \mathbf{r}_e - \mathbf{r}_h$. Since the Keldysh potential is isotropic in the plane it preserves angular momentum, and the second factor in (6) can be written as

$$f(\boldsymbol{\rho}) \equiv f_m(\rho, \phi) = \frac{e^{im\phi}}{\sqrt{2\pi}} \chi_m(\rho), \quad (7)$$

where the integer m is the RM angular momentum quantum number, $\rho \equiv |\boldsymbol{\rho}|$ and ϕ is the azimuthal angle of vector $\boldsymbol{\rho}$. Operating on (6) with H_{e-h} and dividing by the same wavefunction yields the two eigenvalue problems

$$\left[-\left(\frac{\partial^2}{\partial \rho^2} + \frac{1}{\rho} \frac{\partial}{\partial \rho} - \frac{m^2}{\rho^2} \right) + \frac{2\mu}{\hbar^2} (U_K(\rho) - E_f^m) \right] f(\rho) = 0, \quad (8a)$$

$$\left[-\nabla_{\mathbf{R}}^2 + \frac{2M}{\hbar^2} (V_M(\mathbf{R}) - E_F) \right] F(\mathbf{R}) = 0, \quad (8b)$$

with the total energy of state Ψ given by $E = E_F + E_f^m$.

A. The relative motion problem

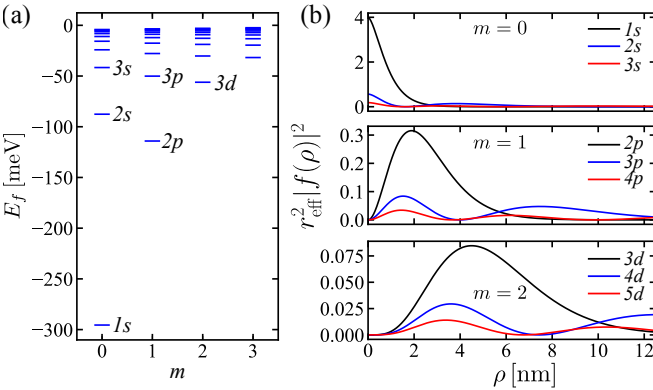


FIG. 2. (a) Binding energies of intralayer excitons in WS₂ on a SiO₂ substrate, as obtained by the direct diagonalization method described in the text. These results are in good agreement with the experiments of Ref. 39. (b) The radial relative-motion wavefunctions corresponding to some of the states shown in (a).

Equation (8a) represents a two-dimensional hydrogenic problem with a non-trivial interaction whose form is logarithmic in the short-range limit⁴⁰, and of Coulomb type at long distances⁴¹. Different approaches have been taken to solve this equation in the context of exciton formation in TMDs, including variational methods³⁸, quantum Monte Carlo simulations^{25,36}, and finite elements calculations²⁵.

Here, we adopt an economical numerical method based on direct diagonalization in a truncated basis, first introduced in nuclear physics⁴², and more recently used in the context of acceptor states in semiconductors^{43–45}. The basis functions

$$\chi_j^m(\rho) \equiv (\beta\rho)^{|m|} e^{-\beta_j \rho}, \quad 1 \leq j \leq N, \quad (9)$$

are inspired by analytical solutions to the 2D hydrogen atom problem⁴¹, and share their general behavior at $\rho = 0$ and $\rho \rightarrow \infty$. Each basis element is defined by its decay length β_j^{-1} , which varies discretely between two values β_N^{-1} and β_1^{-1} . An arbitrary length scale β^{-1} has also been introduced, to make each function dimensionless. We have chosen $\beta_N^{-1} \lesssim r_{\text{eff}} \ll \beta_1^{-1}$ to cover the entire range of Bohr radii that the low-energy excitons are likely to take. The values of β_ℓ are spaced logarithmically as

$$\beta_j = \beta_1 e^{\xi(j-1)}, \quad \xi = (N-1)^{-1} \log(\beta_N/\beta_1), \quad (10)$$

to cover more densely length scales of the order of the screening lengths and below. Then, the radial part of the RM wavefunction can be expanded in this basis as

$$\chi_m(\rho) = \sum_{j=1}^N A_j^m \chi_j^m(\rho). \quad (11)$$

Substituting (11) into (8a), left-multiplying by $\chi_m(\rho)$ and integrating leads to the generalized eigenvalue problem

$$[H^m - E_f S^m] A^m = 0, \quad (12)$$

where we have defined the column vector $A^m = (A_1^m, \dots, A_N^m)^T$, and the matrices H^m and S^m are shown explicitly in Appendix A. Equation (12) is solved numerically to obtain a set of eigenvalues $\{E_f^{m,n}\}$ and eigenvectors $\{A^{m,n}\}$, where n is the principal quantum number.

To test this method, we have evaluated the intralayer exciton spectrum of WS₂ on a SiO₂ substrate by setting $\epsilon = (\epsilon_{\text{vacuum}} + \epsilon_{\text{SiO}_2})/2 = 2.4$, and $r_{\text{eff}} = 2\pi\kappa_{\text{WS}_2}/\epsilon = 15.79 \text{ \AA}$ in Eq. (3). The first few energies and radial wavefunctions are presented in Fig. 2. The obtained values reproduce the non-Rydberg sequence reported experimentally in Ref. 46 and theoretically in Ref. 47. Moreover, the energy spacings between states 1s, 2s and 3s are a good match⁴⁸ to those reported in Ref. 39.

Table II shows our results for the low-energy interlayer excitons in all TMD heterobilayers formed with Mo, W, S and Se, also between a SiO₂ substrate and air/vacuum. The band alignment of each structure, which determines to which material the electron and hole making up the IX belong, has been taken from *ab initio* calculations⁴⁹.

B. The center-of-mass motion problem

The moiré potential V_M appearing in Eq. (8b) has been modeled and parametrized by Yu *et al.* in Ref. 15, based on *ab initio* results for the band-gap and band alignment variation

TABLE II. Calculated binding energies of the lowest-lying interlayer excitons for different semiconducting TMD heterobilayers on a typical SiO₂ substrate. All heterostructures shown have type-II (staggered) band gaps⁴⁹. The electron and hole masses are taken from Table I, according to which layer contains the highest valence-band edge and the lowest conduction-band edge, as reported in Ref. 49.

Heterostructure	Binding energy [meV]					
	1s	2p	2s	3d	3p	3s
MoSe ₂ /MoS ₂	195	100	79	61	53	45
MoSe ₂ /WS ₂	167	78	61	44	39	32
WSe ₂ /MoS ₂	185	94	75	57	50	42
WSe ₂ /MoSe ₂	185	96	76	59	51	43
WSe ₂ /WS ₂	159	75	58	42	37	31
WS ₂ /MoS ₂	199	101	80	61	54	45

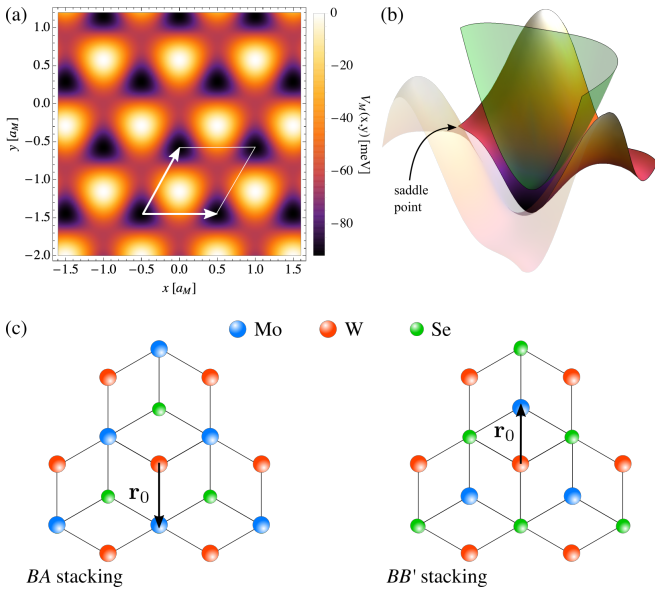


FIG. 3. (a) *Ab initio* moiré potential for interlayer excitons in a fully aligned, *R*-stacked WSe₂/MoSe₂ heterobilayer, as calculated by Yu *et al.*¹⁵ The moiré supercell is shown in white, with the two primitive moiré vectors represented by white arrows. (b) Potential profile around one of the minima, resembling a *C*_{3v}-symmetric harmonic potential below the saddle point energy. Our fitting of this potential well with Eq. (13) is shown in green, offset out of the plane for clarity. (c) Top view of the local stacking configurations at the moiré potential minima for *R*-stacked (*BA*) and *H*-stacked (*BB'*) TMD heterobilayers. In each case, the shortest in-plane vector \mathbf{r}_0 joining the W atom to the M atom is shown.

across different TMD heterobilayers. Fig. 3(a) shows the superlattice potential for interlayer excitons in one such case: *R*-stacked WSe₂/MoSe₂, where at zero twist angle the moiré lattice constant is about 100 nm. The potential landscape contains periodic potential wells interconnected by saddle points and surrounded by three maxima. Each of these wells is *C*_{3v} symmetric about its minimum, and for energies below the saddle point they can be modeled by a simple trigonally-warped

harmonic potential of the form

$$\tilde{V}_M(R, \Phi) = V_0 + \frac{M\omega^2}{2} R^2 [1 - \delta \cos(3\Phi + \varphi)], \quad (13)$$

centered at the well minimum, where R and Φ are the magnitude and polar angle of the COM vector \mathbf{R} , and ω , δ and φ are fitting parameters. This is exemplified in Fig. 3(b). The corresponding fitting parameters for interlayer excitons in this and other TMD heterobilayers are reported in Table III.

TABLE III. Fitting parameters for the model Eq. (13), corresponding to the wells appearing in the moiré potentials reported in Ref. 15, based on DFT calculations. The localized state width R_0 and the barrier energy E_* are also reported.

Heterostructure	$\hbar\omega$ [meV]	δ	R_0 [Å]	E_* [meV]	φ
<i>R</i> -WSe ₂ /MoSe ₂	2.12	0.290	53.64	28	$\pi/2$
<i>H</i> -WSe ₂ /MoSe ₂	1.23	0.292	70.52	14	$-\pi/2$
<i>R</i> -WSe ₂ /MoS ₂	54.83	0.330	10.99	28	$-\pi/2$
<i>H</i> -WSe ₂ /MoS ₂	30.88	0.019	14.65	58	$-\pi/2$

Unlike the true potential V_M , Eq. (13) is unbounded and will always produce localized states, the lowest of which will appear at an energy $E_{F,1} \approx \hbar\omega$ above the potential bottom. Nonetheless, as long as the energy eigenvalue $E_{F,\ell}$ is well below the saddle point energy E_* [see Fig. 3(b)] and the wavefunction decays rapidly enough, the corresponding state will be a good approximation to a localized state of the finite potential well. This is, indeed, the case for *R*-WSe₂/MoSe₂, where $\hbar\omega = 2$ meV is much lower than the saddle point barrier, and the state width, defined by $R_0 = \sqrt{\hbar M^{-1} \omega^{-1}}$, is a full order of magnitude shorter than the moiré superlattice constant (Table III). This suggests that the moiré localized IXs recently reported experimentally by Seyler *et al.*²¹ and Tran *et al.*²² are well described by the potential (13). Incidentally, we note that our estimated values for $\hbar\omega$ are consistent with the shortest energy differences between moiré localized IX resonances reported in Ref. 21 for both *R*- and *H*-stacked WSe₂/MoSe₂. By contrast, the parameters reported in Table III indicate that chalcogen-mismatched heterostructures like WSe₂/MoS₂ may not be well described by this approach, since their moiré periodicities are comparable to the localized state width R_0 . A notable case is *R*-WSe₂/MoS₂, for which $\hbar\omega$ greatly exceeds the saddle-point energy, such that localized IXs are not to be expected in this heterostructure.

To find the energies of IXs localized by the potential (13), we numerically solve the eigenvalue problem (8b) by direct diagonalization over the basis of eigenstates of the 2D harmonic oscillator (2DHO), expressed in cylindrical coordinates as

$$\psi_{j,\mathcal{M}}(R, \Phi) = \frac{e^{i\mathcal{M}\Phi}}{\sqrt{2\pi N_{j,\mathcal{M}}}} \left(\frac{R}{R_0}\right)^{|\mathcal{M}|} e^{-R^2/2R_0^2} L_{\frac{j-|\mathcal{M}|}{2}}^{|\mathcal{M}|} (R^2/R_0^2). \quad (14)$$

Here, L_n^m are associated Laguerre polynomials, and the nor-

malization factors are

$$N_{j,\mathcal{M}} = \frac{R_0^2}{2} \left(\frac{j - |\mathcal{M}|}{2} + 1 \right)_{|\mathcal{M}|}, \quad (15)$$

with $(x)_n = \Gamma(x+n)/\Gamma(x)$ the Pochhammer symbol. The principal quantum number j is a positive integer or zero, and determines the state energy as $E_j^0 = \hbar\omega(j+1)$. The angular momentum quantum number \mathcal{M} is restricted such that $|\mathcal{M}| \leq j$ and $j - |\mathcal{M}|$ is an even number, giving a total degeneracy of $j+1$ for the basis state $\psi_{j,\mathcal{M}}$.

Unlike the case of electron-hole interactions, the C_{3v} -symmetric potential \tilde{V}_M only preserves angular momentum \mathcal{M} modulo 3, and matrix elements between states with different angular momenta must be considered. The appropriate quantum number is then

$$\tilde{\mathcal{M}} = \mathcal{M} \bmod 3, \quad (16)$$

taking the values $-1, 0$ and 1 for states belonging to different irreducible representations (irreps) of group C_{3v} .

Substituting $\psi_{j,\mathcal{M}}$ into Eq. (8b), left-multiplying by $\psi_{j',\mathcal{M}'}$ and integrating, we get the eigenvalue problem

$$[E_F - \hbar\omega(j+1)]\delta_{j',j}\delta_{\mathcal{M}',\mathcal{M}} + \frac{\delta}{4} \frac{\hbar\omega V_{j',j}^{\mathcal{M}',\mathcal{M}} \delta_{|\mathcal{M}'-\mathcal{M}|,3}}{\sqrt{\left(\frac{j'-|\mathcal{M}'|}{2}+1\right)_{|\mathcal{M}'|} \left(\frac{j-|\mathcal{M}|}{2}+1\right)_{|\mathcal{M}|}} = 0. \quad (17)$$

Explicit formulae for $V_{j',j}^{\mathcal{M}',\mathcal{M}}$ are provided in Appendix B. Equation (17) may be divided into three independent blocks with different $\tilde{\mathcal{M}}$ eigenvalue, each of which can be solved numerically by truncating the basis at principal quantum number $j_{\max} \sim 10$, determined by convergence of the low-lying energy eigenvalues. Such convergence is guaranteed, as it can be numerically shown that for any given $\mathcal{M}' = \mathcal{M} \pm 3$, $V_{\mathcal{M}',\mathcal{M}}^{j',j}$ decays rapidly with $|j' - j|$.

Figure 4(a) shows the low-energy spectrum $\{E_F^{\tilde{\mathcal{M}},\ell}\}$ of moiré bound interlayer excitons in R -WSe₂/MoSe₂, as well as the wavefunctions $F_{\tilde{\mathcal{M}},\ell}$ for the first six states. The corresponding energies for this and other TMD heterostructures are listed in Table IV. For simplicity, in both cases we take the potential bottom V_0 as the energy reference. As may be expected by analogy with the isotropic case (2DHO), the ground state, labeled $F_{0,1}$, originates from block $\tilde{\mathcal{M}} = 0$. This state can be viewed as the 2DHO state $\psi_{0,0}$, weakly modified by second-order perturbations from states $\psi_{j \geq 3, \mathcal{M} \pm 3}$, the lowest of which appear $3\hbar\omega$ higher in energy. The perturbative parameter is then $\leq \delta/12 \sim 10^{-2}$, and $E_F^{0,0} \approx \hbar\omega$ to within less than 0.1%. The situation is qualitatively similar for the next two energy levels, a degenerate doublet formed by a state from block $\tilde{\mathcal{M}} = 1$ and one from block $\tilde{\mathcal{M}} = -1$, with energies $E_F^{\pm 1,1} \approx 2\hbar\omega$ to within 5% accuracy. Finally, the 2DHO degenerate triplet formed by $\psi_{2,-2}$, $\psi_{2,0}$ and $\psi_{2,2}$ is split by trigonal warping of the potential into a lower singlet $F_{0,2}$ and a higher degenerate doublet $F_{\pm 1,2}$, separated by a gap of $\approx 0.2\hbar\omega$ or 0.5 meV. Similar level splittings appear for the

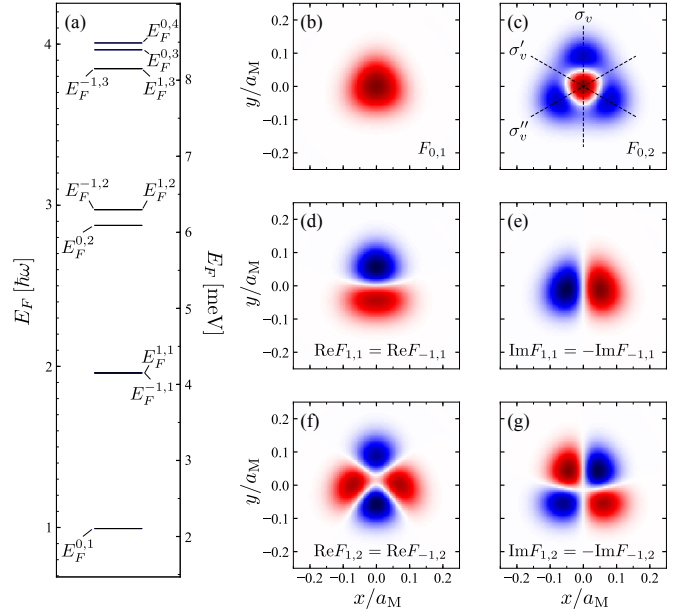


FIG. 4. (a) Spectrum of moiré bound states in R -WSe₂/MoSe₂, shown both in units of $\hbar\omega$ and in meV, according to the parameters reported in Table III. (b)-(g) Wave functions of the six lowest energy states, each normalized to its maximum amplitude for illustration purposes. The x axis has been chosen to cancel out the angle φ in Eq. (13). Blue (red) indicates positive (negative) values, whereas white represents a zero value. According to their properties under C_3 rotations and mirror reflections about the axes shown in panel (c), modes $F_{0,0}$ and $F_{0,1}$ are associated to the A_1 irrep, and $F_{\pm 1,0}$ and $F_{\pm 1,1}$ to the E irrep of the point group C_{3v} of the potential (13).

entire spectrum from this point on. By comparison, Ref. 21 reports IX photoluminescence (PL) peaks as narrow as $100 \mu\text{eV}$, indicating that experimental observation of the predicted broken degeneracies is currently possible. The same sequence of quantum numbers is found also for H -WSe₂/MoSe₂ and H -WSe₂/MoS₂, as reported in Table IV.

TABLE IV. Calculated energies of the lowest-lying moiré localized IXs in different semiconducting TMD heterobilayers. All energies are measured with respect to the corresponding potential well bottom V_0 in Eq. (13). For H -WSe₂/MoS₂ only the first energy is below the saddle-point barrier.

Heterostructure	Localized IX energy [meV]					
	$E_F^{0,1}$	$E_F^{\pm 1,1}$	$E_F^{0,2}$	$E_F^{\pm 1,2}$	$E_F^{\pm 1,3}$	$E_F^{0,3}$
R -WSe ₂ /MoSe ₂	2.105	4.153	6.095	6.303	8.158	8.406
H -WSe ₂ /MoSe ₂	1.221	2.410	3.535	3.656	4.731	4.876
H -WSe ₂ /MoS ₂	30.877	61.754	92.621	92.637	123.498	123.517

The six wavefunctions discussed above are plotted in Figures 4(b)-(g). From inspection of their symmetries⁵⁰, we deduce that $F_{0,1}$ and $F_{0,2}$ transform according to the one-dimensional irrep A_1 of group C_{3v} . That is, $F_{0,1}$ and $F_{0,2}$ do not acquire a phase under C_3 rotations or mirror operations about

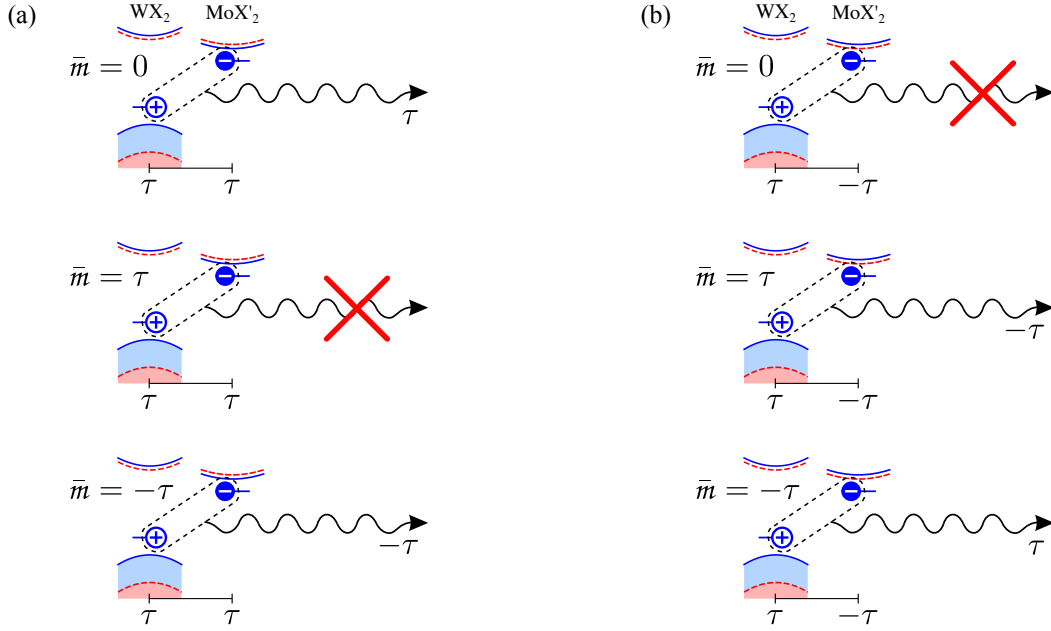


FIG. 5. Selection rules for the photoluminescence of s -type ($m = 0$) moiré localized IXs in (a) R -type and (b) H -type TMD heterobilayers. In all diagrams the exciton is depicted as a mid-gap level for the electron and the hole, and the emitted photon as a wavy line. Red crosses indicate that the IX state is forbidden by symmetry to decay into an in-plane-polarized photon.

the axes sketched in Fig. 4(c). Similarly, the degenerate doublets $F_{\pm 1,1}$ and $F_{\pm 1,2}$ belong to the two-dimensional irrep E . In general, we find that degenerate states of irrep E originate from the $\bar{\mathcal{M}} = \pm 1$ blocks, whereas the $\bar{m} = 0$ block produces states belonging to A_1 and A_2 . The first two states belonging to the latter are $F_{0,3}$ and $F_{0,6}$, which acquire a (-1) phase factor under mirror operations (see Fig. 9 in Appendix D). While IXs are—due to their permanent electric dipole moment—mainly susceptible to out-of-plane electric fields, the in-plane symmetry of the wavefunctions shown in Fig. 4 will determine the localized IX's interaction with perturbations such as impurities with non trivial symmetry properties, as well as phonons.

III. SYMMETRY CONSIDERATIONS AND OPTICAL SELECTION RULES

Having computed the RM and COM parts of the wave function, we are now in a position to construct the full excitonic state. For COM quantum numbers $(\bar{\mathcal{M}}, \ell)$ and RM quantum numbers (m, n) , and taking the bottom of the moiré potential well as the origin of coordinates, the localized IX wave function is given by

$$|\text{IX}_{\tau', \tau}^{c', v; s} \rangle_{\bar{\mathcal{M}}, \ell}^{m, n} = \int d^2 r_e \int d^2 r_h e^{i(\tau' \mathbf{K}' \cdot \mathbf{r}_e - \tau \mathbf{K} \cdot \mathbf{r}_h)} \Psi_{\bar{\mathcal{M}}, \ell}^{m, n}(\mathbf{r}_e, \mathbf{r}_h) \times \varphi_{c', \tau', s}^\dagger(\mathbf{r}_e) \varphi_{v, \tau, s}(\mathbf{r}_h) |\Omega\rangle, \quad (18)$$

where $\varphi_{\alpha, \tau, s}(\mathbf{r})$ is the field operator for an electron of band α with spin and valley quantum numbers s and τ , respectively; \mathbf{K} (\mathbf{K}') is the valley vector MX₂ ($\text{M}'\text{X}'_2$); and $|\Omega\rangle$ represents

the charge-neutral many-body ground state. The two-body state (18) is formed by an electron and a hole of opposite spin projections, and thus can recombine in the absence of spin-flip mechanisms^{51,52}, which we shall ignore in our discussion. In addition, we shall restrict the relative values of τ and τ' in order to form exciton states that can recombine without intervalley scattering. This is achieved by setting $\tau' = \tau$ for configurations close to R stacking, and $\tau' = -\tau$ for cases close to H stacking. The optical activity of excitons that meet these criteria is then solely dependent on the symmetry properties of the exciton state, which we address next.

In Sec. II B we have identified the relation between $\bar{\mathcal{M}}$ and the COM states' irreducible representation, which immediately yields the symmetry rules

$$\begin{aligned} C_3 F_{\bar{\mathcal{M}}, \ell} &= e^{-i \frac{2\pi}{3} \bar{\mathcal{M}}} F_{\bar{\mathcal{M}}, \ell}, \\ C_3 f_{m, n} &= e^{-i \frac{2\pi}{3} m} f_{m, n}, \\ C_3 \Psi_{\bar{\mathcal{M}}, \ell}^{m, n} &= e^{-i \frac{2\pi}{3} (\bar{\mathcal{M}} + m)} \Psi_{\bar{\mathcal{M}}, \ell}^{m, n}, \end{aligned} \quad (19)$$

where the second expression stems trivially from Eq. (7). Using Eq. (19), it can be shown that (18) transforms under C_3 rotations as (Appendix C)

$$C_3 |\text{IX}_{\tau', \tau}^{c', v; s} \rangle_{\bar{\mathcal{M}}, \ell}^{m, n} = e^{-i \frac{2\pi}{3} (\bar{\mathcal{M}} + m)} \phi_{\Omega} \phi_{c', \tau'} \phi_{v, \tau}^* |\text{IX}_{\tau', \tau}^{c', v; s} \rangle_{\bar{\mathcal{M}}, \ell}^{m, n}, \quad (20)$$

with $\phi_{c', \tau'}$, $\phi_{v, \tau}$ and ϕ_{Ω} the C_3 eigenvalues of the conduction- and valence-band Bloch functions and the state $|\Omega\rangle$, respectively.

The values of $\phi_{c', \tau'}$ and $\phi_{v, \tau}$ are determined by the local interlayer registry at the bottom of the potential well⁵³. In

the case of $R\text{-WSe}_2/\text{MoSe}_2$ ($\tau' = \tau$), this corresponds to BA stacking [Fig. 3(c)], where the W atom of the WSe_2 layer is aligned with the hollow site of the MoSe_2 layer, while Se atoms in the WSe_2 layer coincide with the Mo atoms of MoSe_2 . By contrast, for $H\text{-WSe}_2/\text{MoSe}_2$ and $H\text{-WSe}_2/\text{MoS}_2$ ($\tau' = -\tau$) the local stacking is BB' [Fig. 3(d)], where once again the W atom aligns with the MoSe_2 hollow site, while the chalcogens in both layers coincide. In both cases, we may take the bottom-layer W atom as the common rotation center, such that the electron Bloch function rotates about the top-layer hollow site, resulting in⁵³

$$\phi_{v,\tau} = e^{i\frac{2\pi\tau}{3}}, \quad (21a)$$

$$\phi_{c',\tau'} = e^{-i\frac{2\pi\tau'}{3}} = \begin{cases} e^{-i\frac{2\pi\tau}{3}}, & R \text{ stacking} \\ e^{i\frac{2\pi\tau}{3}}, & H \text{ stacking} \end{cases}. \quad (21b)$$

This finally gives

$$C_3 |IX_{\tau',\tau}^{c',v;s}\rangle_{\tilde{m},\ell}^{m,n} = \begin{cases} e^{-i\frac{2\pi}{3}(\tilde{M}+m-\tau)} \phi_{\Omega} |IX_{\tau',\tau}^{c',v;s}\rangle_{\tilde{m},\ell}^{m,n}, & R \text{ stacking} \\ e^{-i\frac{2\pi}{3}(\tilde{M}+m)} \phi_{\Omega} |IX_{\tau',\tau}^{c',v;s}\rangle_{\tilde{m},\ell}^{m,n}, & H \text{ stacking} \end{cases}. \quad (22)$$

Optical transitions are possible only between states with the same C_3 eigenvalue. For a state

$$|\eta, \xi\rangle = a_{\eta}^{\dagger}(\xi)|\Omega\rangle, \quad (23)$$

where the boson operator $a_{\eta}^{\dagger}(\xi)$ creates a single photon of wave vector ξ and in-plane circular polarization $\eta = \pm 1$ (for right- and left-handed, respectively), the corresponding C_3 eigenvalue is $\phi_{\Omega} e^{i\frac{2\pi}{3}\eta}$. The optical selection rules for localized IXs and in-plane polarized photons are then summarized as

$$\eta = \begin{cases} (\tau - \tilde{M} - m) \bmod 3, & R \text{ stacking} \\ -(\tilde{M} + m) \bmod 3, & H \text{ stacking} \end{cases}, \quad (24)$$

and illustrated in Fig. 5 for $m = 0$ in the context of photoluminescence. In R -type structures [Fig. 5(a)], $\tilde{M} = 0$ states at valley τ produce PL of polarization $\eta = \tau$, opposite to the well known selection rule for intralayer excitons ($\eta = -\tau$), as recently reported by Seyler *et al.*²¹ and Tran *et al.*²², whereas states with $\tilde{M} = -\tau$ give PL of polarization $\eta = -\tau$. For $\tilde{M} = \tau$ the IX C_3 eigenvalue is one, which is incompatible with the two possible values of η ; these states are dark for in-plane polarized photons, and couple instead to out-of-plane polarized ones that propagate along the heterostructure plane. Since these photons are missed by most optical experiments⁵¹, we label them as “dark”. Moving on to the case of H -type structures [Fig. 5(b)], we find that the optical selection rules are valley independent, since the valley-dependent orbital angular momenta of the electron and hole Bloch states cancel each other out. Equation (24) shows that $\tilde{M} = 0$ states at either valley are dark, while $\tilde{M} \neq 0$ states produce PL of polarization $\eta = -\tilde{M}$.

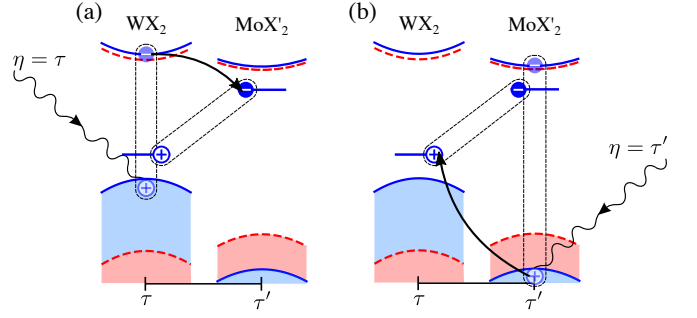


FIG. 6. Photon absorption processes for moiré localized interlayer excitons in the TMD heterobilayer $H\text{-WX}_2/\text{MoX}'_2$. Bands of different spin are shown in different colors. The incoming photon (wavy line) interacts with either (a) the WX_2 or (b) the MoX'_2 layer to create an intralayer exciton. In the former case, the electron may tunnel into MoX'_2 to form the localized IX state. Alternatively, in the latter case the hole may tunnel into WX_2 to form the same IX state.

IV. ABSORPTION SPECTRUM OF MOIRÉ LOCALIZED INTERLAYER EXCITONS

Due to the spatial separation between their constituting carriers, direct interaction of IXs with light is weak^{24,54}, and the IX oscillator strength comes mainly from mixing with bright intralayer excitons^{18,24}. Such mixing can be taken into account perturbatively, given the weak tunneling strengths and large interlayer CB and VB detunings^{37,49} typical of type-II TMD heterostructures⁵⁵. The dominant contributions to the photon absorption rate are given by the two processes sketched in Fig. 6, where an incoming photon, depicted as a wavy line, is shown to interact with either of the two TMD layers to create a *virtual* intralayer exciton. Then, one of the two carriers can tunnel into the opposite layer to form a moiré localized IX, shown as mid-gap levels for the electron and the hole.

This process introduces additional constraints on top of the selection rules obtained in Sec. III. Firstly, formation of the intermediate exciton state in either layer is constrained by the intralayer optical selection rule $\eta = -\tau$ if it forms in the MX_2 layer, or $\eta = -\tau'$ if it forms in the $\text{M}'\text{X}'_2$ layer. Moreover, the intermediate exciton must have an angular momentum quantum number³⁹ $m = 0$, which sets the same quantum number for the moiré localized IX. In other words, s -type IXs will dominate the absorption spectrum associated to moiré localized excitons.

To compute the probability amplitudes of the processes in Fig. 6, we first evaluate the corresponding mixed intralayer-interlayer exciton wavefunction, to first order in perturbation

TABLE V. Energies of A ($\tau s = -1$) and B ($\tau s = +1$) intra- and interlayer excitons in $\text{WSe}_2/\text{MoSe}_2$, relevant to photon absorption through the processes of Fig. 6. The A -exciton energies were extracted from Refs. 21 and 22. The B -exciton values were estimated by adding the experimental spin-orbit splittings reported in Ref. 34 to the A -exciton energies.

	A exc. energy [eV]			B exc. energy [eV]		
	$\bar{n} = 1$	$\bar{n} = 2$	$\bar{n} = 3$	$\bar{n} = 1$	$\bar{n} = 2$	$\bar{n} = 3$
WSe_2	1.715 ^{a,b}	1.837	1.872	2.163 ^{a,b}	2.285	2.320
MoSe_2	1.630 ^a	1.758	1.796	1.871	1.999	2.037
	R stacking [eV]			H stacking [eV]		
	IX			1.320 ^a		
	1.320 ^a			1.392 ^a		

^aReference [21], ^bReference [22]

theory:

$$\begin{aligned}
|\text{hX}_{\tau',\tau}^{c',v;s}\rangle_{\bar{\mathcal{M}},\ell}^{0,n} &= |\text{IX}_{\tau',\tau}^{c',v;s}\rangle_{\bar{\mathcal{M}},\ell}^{0,n} \\
&+ \sum_{\mathbf{Q},\bar{n}} \frac{\langle \text{X}_{\tau,\tau}^{c,v;s}(\mathbf{Q}) | H_T | \text{IX}_{\tau',\tau}^{c',v;s}\rangle_{\bar{\mathcal{M}},\ell}^{0,n}}{E_{\bar{\mathcal{M}},\ell,\tau}^{0,n;s} - E_{\tau,\bar{n};s}(\mathbf{Q})} |\text{X}_{\tau,\tau}^{c,v;s}(\mathbf{Q})\rangle_{\bar{n}} \\
&+ \sum_{\mathbf{Q},\bar{n}} \frac{\langle \text{X}_{\tau',\tau'}^{c',v';s}(\mathbf{Q}) | H_T | \text{IX}_{\tau',\tau}^{c',v;s}\rangle_{\bar{\mathcal{M}},\ell}^{0,n}}{E_{\bar{\mathcal{M}},\ell,\tau}^{0,n;s} - E'_{\tau',\bar{n};s}(\mathbf{Q})} |\text{X}_{\tau',\tau'}^{c',v';s}(\mathbf{Q})\rangle_{\bar{n}},
\end{aligned} \quad (25)$$

where $|\text{X}_{\tau,\tau}^{c,v}(\mathbf{Q})\rangle_{\bar{n}}$ and $|\text{X}_{\tau',\tau'}^{c',v'}(\mathbf{Q})\rangle_{\bar{n}}$ are the wave functions of s -type intralayer excitons with COM wave vector \mathbf{Q} in MX_2 and $\text{M}'\text{X}'_2$, respectively. We have also introduced the intralayer exciton dispersions

$$\begin{aligned}
E_{\tau,\bar{n};s}(\mathbf{Q}) &= E_{\tau s;\bar{n}}^0 + \frac{\hbar^2 Q^2}{2(m_e + m_h)}, \\
E'_{\tau',\bar{n};s}(\mathbf{Q}) &= E_{\tau' s;\bar{n}}^0 + \frac{\hbar^2 Q^2}{2(m_{e'} + m_{h'})},
\end{aligned} \quad (26)$$

with m_e and $m_{h'}$ are the electron and hole masses in the MX_2 and $\text{M}'\text{X}'_2$ layers, respectively. The interlayer tunneling Hamiltonian for the moiré heterostructure is^{18,56}

$$\begin{aligned}
H_T &= \sum_s \sum_{\eta=0}^2 \sum_{\tau,\tau'} \sum_{\mathbf{k},\mathbf{k}'} \delta_{\mathbf{k}-\mathbf{k}',C_3^\eta \Delta \mathbf{K}_{\tau'\tau}} e^{i\tau C_3^\eta \mathbf{K} \cdot \mathbf{r}_0} \left[t_c c_{c',\tau',s}^\dagger(\mathbf{k}') c_{c,\tau,s}(\mathbf{k}) \right. \\
&\quad \left. + t_v e^{i\frac{2\pi\eta}{3}(\tau-\tau')} c_{v',\tau',s}^\dagger(\mathbf{k}') c_{v,\tau,s}(\mathbf{k}) \right] + \text{H.c.},
\end{aligned} \quad (27)$$

where $\Delta \mathbf{K}_{\tau'\tau} = \tau' \mathbf{K}' - \tau \mathbf{K}$ is the interlayer valley mismatch; t_c and t_v are hopping parameters; and \mathbf{r}_0 is the shortest in-

plane vector joining the metal atoms of the two layers at the localization site. For BA and BB' stacking we have $\mathbf{r}_0^{\text{BA}} = -\mathbf{r}_0^{\text{BB}'} = -\frac{a_{\text{WSe}_2}}{\sqrt{3}} \hat{\mathbf{y}}$; these vectors are shown in Fig. 3(c).

$E_{\tau s;\bar{n}}^0$ and $E_{\tau' s;\bar{n}}^0$ in Eq. (26) are given by the corresponding intralayer band gaps and binding energies, as obtained in Sec. II A. Instead, we choose to extract the values of $E_{\tau s;1}^0$ and $E_{\tau' s;1}^0$ from experiments^{21,22}: for $\tau s = -1$, these correspond to the A exciton in the respective layer, whereas for $\tau s = 1$ the energies refer to the B exciton. The full series of states can then be estimated by combining these experimental values with the level spacings predicted by our method of Sec. II A. We follow the same strategy for the IX, writing $E_{\bar{\mathcal{M}},\ell,\tau}^{0,n;s} = E_{\tau',\tau;s}^0 + E_F^{\bar{\mathcal{M}},\ell}$. The reference energy $E_{\tau',\tau;s}^0$ was taken from Ref. 21, using the lowest measured localized state energy for R stacking as $E_{1,1;\downarrow}$, and the same for H stacking as $E_{-1,1;\downarrow}$. The compiled results are shown in Table V, including intralayer exciton states with $\bar{n} = 1, 2$ and 3.

Next, we compute the decay rate of state (23) into every possible weakly hybridized exciton (25) with Fermi's golden rule

$$\Gamma_\eta(\xi) = \frac{2\zeta}{\hbar} \sum_{\bar{\mathcal{M}},\ell,n} \sum_{\tau,s} \frac{|\langle \eta, \xi | H_{\text{LM}} | \text{hX}_{\tau',\tau}^{c',v;s}\rangle_{\bar{\mathcal{M}},\ell}^{0,n}|^2}{(\hbar c \xi - E_{\bar{\mathcal{M}},\ell,\tau}^{0,n;s})^2 + \zeta^2}, \quad (28)$$

with a relaxed energy conservation condition to allow for a phenomenological Lorentzian broadening ζ caused by impurities and disorder. The light-matter interaction Hamiltonian is

$$\begin{aligned}
H_{\text{LM}} &= \frac{e\gamma}{\hbar c} \sum_{s,\eta} \sum_{\mathbf{k},\xi} \sqrt{\frac{4\pi\hbar c}{SL\xi}} c_{c,\eta,s}^\dagger(\mathbf{k} + \xi_\parallel) c_{v,\eta,s}(\mathbf{k}) a_{-\eta}(\xi) \\
&+ \frac{e\gamma'}{\hbar c} \sum_{s,\eta} \sum_{\mathbf{k},\xi} \sqrt{\frac{4\pi\hbar c}{SL\xi}} c_{c',\eta,s}^\dagger(\mathbf{k} + \xi_\parallel) c_{v',\eta,s}(\mathbf{k}) a_{-\eta}(\xi) + \text{H.c.},
\end{aligned} \quad (29)$$

with γ (γ') the matrix element of the in-plane momentum operator between the WSe_2 (MoSe_2) conduction and valence bands at the \mathbf{K} (\mathbf{K}') point.

Finally, the absorption rate $A_\eta(\varepsilon)$ for photons of energy ε and circular polarization η can be estimated by multiplying (28) by the number of localizing centers per unit area—one per moiré unit cell—and by the number of available photon states within a range $\Delta\varepsilon$ of that energy¹⁸, which may be identified with the energy resolution of the measurement. For simplicity, we consider only $1s$ states for both the localized IX and the virtual intralayer excitons [$\bar{n} = n = 1$ in the sum of Eq. (28)]. This gives

$$A_\eta(\varepsilon) = \frac{e^2}{\hbar c} \frac{16\varepsilon\Delta\varepsilon}{\sqrt{3}a_M^2\hbar^3c^2} \sum_{s,\tau} \sum_{\bar{\mathcal{M}},\ell} \left| \sum_{\mu=0}^2 \Phi_{\bar{\mathcal{M}},\ell}^{\tau',\tau,\mu} \left(\gamma t_c \frac{X_{\tau,\tau;1}^{c,v*}(0) I_\tau}{E_{\bar{\mathcal{M}},\ell,\tau}^{0,1;s} - E_{\tau s;1}^0} \delta_{\eta,-\tau} - \gamma' t_v \frac{e^{i\frac{2\pi}{3}(\tau-\tau')\mu} X_{\tau',\tau';1}^{c',v'*}(0) I_{\tau'}}{E_{\bar{\mathcal{M}},\ell,\tau}^{0,1;s} - E_{\tau' s;1}^0} \delta_{\eta,-\tau'} \right) \right|^2 \frac{1}{\pi} \frac{\zeta}{(\varepsilon - E_{\bar{\mathcal{M}},\ell,\tau}^{0,1;s})^2 + \zeta^2}, \quad (30)$$

where $X_{\tau,\bar{n}}^{c,v}(\rho)$ and $X_{\tau',\bar{n}}^{c',v'}(\rho)$ are the MX_2 and $\text{M}'\text{X}'_2$ intralayer exciton real-space RM wave functions, and we have defined

$$\begin{aligned}\Phi_{\bar{M},\ell}^{\tau,\tau,\mu} &= \tilde{F}_{\bar{M},\ell}(-C_3^\mu \Delta \mathbf{K}_{\tau,\tau}) e^{-i\tau C_3^\mu \mathbf{K} \cdot \mathbf{r}_0}, \\ I_\tau &= \int d^2\rho X_{\tau,\tau;1}^{c,v*}(\rho) f_{0,1}(\rho), \\ I'_{\tau'} &= \int d^2\rho X_{\tau',\tau';1}^{c',v'*}(\rho) f_{0,1}(\rho).\end{aligned}\quad (31)$$

The intra- and interlayer exciton RM wave functions were computed using the numerical method of Sec. II A, and numerically integrated to evaluate I_τ and $I'_{\tau'}$.

A. Optical selection rules for absorption

Equation (30) encodes the optical selection rules for absorption through the processes of Fig. 6. We begin with the case of H -stacked structures, where the individual layer contributions to absorption are

$$\begin{aligned}A_{\eta=-\tau}^{(H)} &= \frac{e^2}{\hbar c} \frac{16\varepsilon\Delta\varepsilon |\gamma|^2 t_c^2 |X_{\tau,\tau;1}^{c,v*}(0)|^2}{\sqrt{3}a_M^2 h^3 c^2} \sum_{\bar{M},\ell,s} \left| \frac{I_\tau}{E_{\bar{M},\ell,\tau}^{0,1;s} - E_{\tau s;1}^0} \right|^2 \\ &\times \left| \sum_{\mu=0}^2 \Phi_{\bar{M},\ell}^{-\tau,\tau,\mu} \right|^2 \frac{\zeta/\pi}{(\varepsilon - E_{\bar{M},\ell,\tau}^{0,1;s})^2 + \zeta^2},\end{aligned}\quad (32a)$$

$$\begin{aligned}A_{\eta=\tau}^{(H)} &= \frac{e^2}{\hbar c} \frac{16\varepsilon\Delta\varepsilon |\gamma|^2 t_v^2 |X_{\tau,\tau;1}^{c',v*}(0)|^2}{\sqrt{3}a_M^2 h^3 c^2} \sum_{\bar{M},\ell} \left| \frac{I'_{-\tau}}{E_{\bar{M},\ell,\tau}^{0,1;s} - E_{-\tau s;1}^0} \right|^2 \\ &\times \left| \sum_{\mu=0}^2 \Phi_{\bar{M},\ell}^{-\tau,\tau,\mu} e^{-i\frac{2\pi}{3}\tau\mu} \right|^2 \frac{\zeta/\pi}{(\varepsilon - E_{\bar{M},\ell,\tau}^{0,1;s})^2 + \zeta^2}.\end{aligned}\quad (32b)$$

In each case, the sum over μ can be simplified by noting that $\tilde{F}_{\bar{M},\ell}(C_3\mathbf{q}) = e^{i\frac{2\pi}{3}\bar{M}} \tilde{F}_{\bar{M},\ell}(\mathbf{q})$, yielding the same rule for $\Phi_{\bar{M},\ell}^{\tau',\tau}$. This gives

$$\begin{aligned}\sum_{\mu=0}^2 \Phi_{\bar{M},\ell}^{-\tau,\tau,\mu} &= \tilde{F}_{\bar{M},\ell}(-\Delta \mathbf{K}_{-\tau,\tau}) \\ &\times [1 + 2\cos\{\frac{2\pi}{3}(\bar{M} - \tau)\}],\end{aligned}\quad (33a)$$

$$\begin{aligned}\sum_{\mu=0}^2 \Phi_{\bar{M},\ell}^{-\tau,\tau,\mu} e^{-i\frac{2\pi}{3}\tau\mu} &= \tilde{F}_{\bar{M},\ell}(-\Delta \mathbf{K}_{-\tau,\tau}) \\ &\times [1 + 2\cos\{\frac{2\pi}{3}(\bar{M} + \tau)\}].\end{aligned}\quad (33b)$$

Expressions (33a) and (33b) give a finite contribution to absorption by the MX_2 layer only for $\bar{M} = \tau = -\eta$, whereas the $\text{M}'\text{X}'_2$ layer contributes only for $\bar{M} = \tau' = -\eta$, making

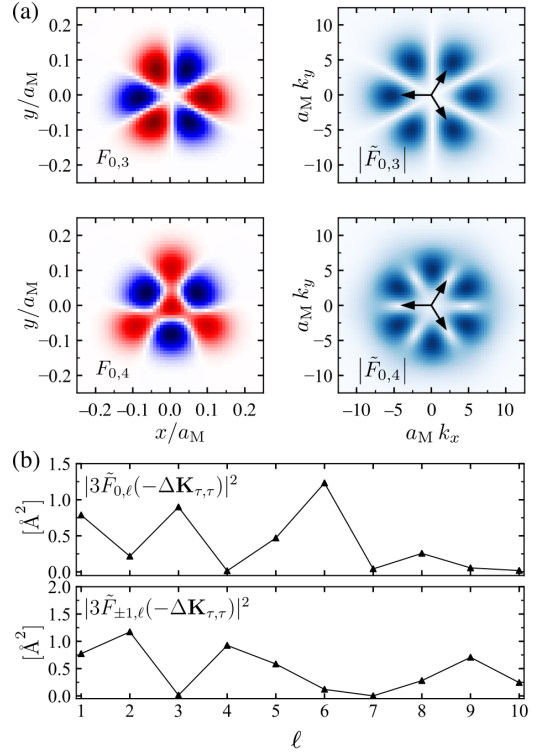


FIG. 7. (a) Moiré localized IX wavefunctions $F_{0,\ell}$ and the moduli of their Fourier transforms $|\tilde{F}_{0,\ell}|$ for $\ell = 2$ and 3 in R -WSe₂/MoSe₂. The arrows plotted in the right panels correspond to the three vectors $-C_3^\mu \Delta \mathbf{K}_{\tau,\tau}$, with $\mu = 0, 1, 2$ and $\tau = 1$. (b) The weighting factor $|3\tilde{F}_{\pm 1,\ell}(-\Delta \mathbf{K}_{1,1})|^2$ as a function of ℓ for $\bar{M} = 0$ (top) and $\bar{M} = 1$ (bottom), evaluated for the same heterobilayer.

$\bar{M} = 0$ states dark. These results are in full agreement with the selection rules of Eq. (24), and correspond to the middle and lower panels of Fig. 5(b).

For R stacking, the two layer-polarized processes interfere to give the absorption rate

$$\begin{aligned}A_{\eta=-\tau}^{(R)}(\varepsilon) &= \frac{e^2}{\hbar c} \frac{16\varepsilon\Delta\varepsilon}{\sqrt{3}a_M h^3 c^2} \sum_{\bar{M},\ell,s} \left| \sum_{\mu=0}^2 \Phi_{\bar{M},\ell}^{\tau,\tau,\mu} \right|^2 \frac{\zeta/\pi}{(\varepsilon - E_{\bar{M},\ell,\tau}^{0,1;s})^2 + \zeta^2} \\ &\times \left| \gamma t_c \frac{X_{\tau,\tau;1}^{c,v*}(0) I_\tau}{E_{\bar{M},\ell,\tau}^{0,1;s} - E_{\tau,1;s}^0} - \gamma t_v \frac{X_{\tau,\tau;1}^{c',v*}(0) I'_\tau}{E_{\bar{M},\ell,\tau}^{0,1;s} - E'_{\tau,1;s}} \right|^2,\end{aligned}\quad (34)$$

where we have

$$\sum_{\mu=0}^2 \Phi_{\bar{M},\ell}^{\tau,\tau,\mu} = \tilde{F}_{\bar{M},\ell}(-\Delta \mathbf{K}_{\tau,\tau}) [1 + 2\cos\{\frac{2\pi}{3}(\bar{M} + \tau)\}]. \quad (35)$$

Expression (35) is non zero only for $\bar{M} = -\tau = \eta$ in agreement with Eq. (24), corresponding to the inverse process to that in the bottom panel of Fig. 5(a). Though allowed by symmetry in R -stacked structures, absorption by $\bar{M} = 0$ states cannot be mediated by intralayer excitons, as it violates the intralayer optical selection rules.

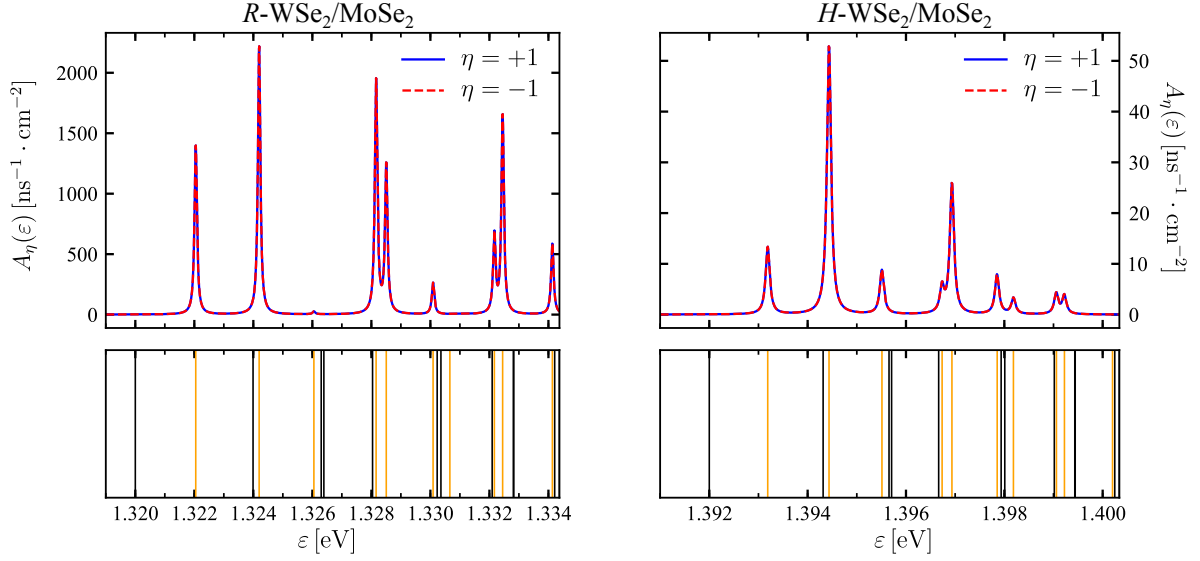


FIG. 8. Absorption rate per unit area of moiré localized IXs in R -WSe₂/MoSe₂ (left panel) and H -WSe₂/MoSe₂ (right panel), for right- ($\eta = +1$) and left-handed ($\eta = -1$) polarized light. The bottom panels show the corresponding calculated IX spectra, with $\mathcal{M} = 0$ ($\mathcal{M} = \pm 1$) states represented by black (orange) lines. The absolute IX energies are based on the experimental values reported in Table V combined with our numerical results, and we have used phenomenological $\beta = 50 \mu\text{eV}$ line widths for the absorption resonances, a detector resolution $\Delta\epsilon = 50 \mu\text{eV}$, and hopping strengths $t_v = 2t_c = 52 \text{ meV}$.

The above analysis leads to the important conclusion that the dominant absorption processes favor localized IXs of the E irrep of group C_{3v} , by contrast to more homogeneous states on which most interpretations of the optics of localized moiré IXs have been based thus far^{15,52}. The symmetry properties of these states are expected to play an important role when considering how they are influenced by impurities and other perturbations, as well as possible means to modify their optical response.

B. Numerical results

Equations (33a), (33b) and (35) show that the localized IX's oscillator strength is determined by the Fourier transform of the COM wave function evaluated at a single wave vector $-\Delta\mathbf{K}_{\tau',\tau}$. Note that, while the latter vector is determined by the moiré supercell vectors [Fig. 3(a)], the wave function $F_{\tilde{\mathcal{M}},\ell}$ is given by the trigonally symmetric potential well, whose orientation in the moiré pattern is given by the phase factor φ appearing in Eq. (13).

Figure 7(a) shows two sample functions $\tilde{F}_{0,3}$ and $\tilde{F}_{0,4}$ for R -WSe₂/MoSe₂, with arrows indicating the vectors $-C_3^\mu \Delta\mathbf{K}_{1,1}$. In the former case the three vectors coincide with lobes of the function, giving a finite oscillator strength, whereas in the latter they align with nodes, resulting in a dark state. Figure 7(b) shows the corresponding prefactors $|3\tilde{F}_{\tilde{\mathcal{M}},\ell}(-\Delta\mathbf{K}_{1,1})|^2$ for the first few localized IXs, indicating that the states with $\tilde{\mathcal{M}} = 0$ and $\ell = 7$ and $\ell = 10$, and those with $\tilde{\mathcal{M}} = \pm 1$ and $\ell = 3, 7$ and 10 are also dark. This effect is, in a sense, accidental, as it is independent of the potential well symmetry. Further *ab ini-*

tio studies of TMD heterostructures are necessary to ascertain whether different pairs of TMDs will produce the same moiré potential landscape for IXs when similarly stacked into a heterostructure. Here, we simply focus on the cases of R - and H -stacked WSe₂/MoSe₂, which we consider to be of interest for experiments.

Figure 8 shows the polarization-resolved absorption spectra of moiré localized IXs in R - and H -stacked WSe₂/MoSe₂. The curves were constructed based on the selection rules of Sec. IV A, our numerical results for $\tilde{F}_{\tilde{\mathcal{M}},\ell}(-\Delta\mathbf{K}_{\tau',\tau})$, and the experimental data of Table V. For the tunnelling strengths entering Eq. (27), we use $t_v = 2t_c = 52 \text{ meV}$ motivated by earlier work on TMD heterobilayers^{10,18}, which should suffice for an order-of-magnitude estimation. The corresponding localized IX spectra are shown in the bottom panels to highlight the absence of absorption signatures from $\mathcal{M} = 0$ states, as dictated by symmetry, as well as from some $\tilde{\mathcal{M}} \neq 0$ states for which $F_{\tilde{\mathcal{M}},\ell}(-\Delta\mathbf{K}_{\tau',\tau}) \approx 0$. The absorption profiles for right- and left-circularly polarized light are identical, as guaranteed by time reversal symmetry.

V. CONCLUSIONS

We have presented an in-depth study of interlayer exciton localization by trigonally symmetric moiré potentials in type-II transition-metal dichalcogenide heterostructures. Our numerical results for the localized exciton spectra are in good qualitative agreement with recent experiments²¹, and the associated wave functions have allowed us to identify each state's symmetry properties as inherited from the localizing potential and the carrier Bloch functions. We have derived general

optical selection rules for such states that generalize early theoretical descriptions¹⁵, and which are in full agreement with experimental results^{21,22}. By pairing these rules with the dominant exciton-photon interaction processes, we have predicted that the moiré-localized-state sector of the optical absorption in these materials is dominated by states belonging to the E irreducible representation of the group C_{3v} . These results are fundamental to understanding how general perturbations influence moiré localized exciton states, and lay the groundwork for the manipulation of their optical response.

ACKNOWLEDGMENTS

All authors acknowledge funding from DGAPA-UNAM, through projects PAPIIT no. IN113920 and PAPIME PE107219. D.A.R.-T. and F.M. acknowledge the support

of DGAPA-UNAM through its postdoctoral fellowships program. D.A.R.-T. thanks M. Danovich for many fruitful discussions on the present subject. I.S. thanks the hospitality of CNyN-UNAM during the event *Escuela Nacional de Nanociencias 2019*, where this project was conceived.

Appendix A: Matrix elements of the relative motion problem

Taking the basis states of (9), the RM Hamiltonian matrix elements can be written as

$$H_{jj'}^m = K_{jj'}^m - \frac{2\mu e^2}{\hbar^2 \epsilon r_{\text{eff}}} U_{jj'}^m, \quad (\text{A1})$$

with auxiliary matrix elements

$$K_{jj'}^m \equiv \int_0^\infty d\rho \rho \chi_j^{m*}(\rho) \left[\frac{\partial^2}{\partial \rho^2} + \frac{1}{\rho} \frac{\partial}{\partial \rho} - \frac{m^2}{\rho} \right] \chi_{j'}^m(\rho) = -[2|m|+1] \frac{\beta^{2|m|} \beta_j}{(\beta_j + \beta_{j'})^{2|m|+1}} \Gamma(2|m|+1) + \frac{\beta^{2|m|} \beta_j^2}{(\beta_j + \beta_{j'})^{2|m|+2}} \Gamma(2|m|+2), \quad (\text{A2a})$$

$$U_{jj'}^m \equiv \frac{\pi}{2} \int_0^\infty d\rho \rho \chi_j^{m*}(\rho) \left[H_0 \left(\frac{\rho}{r_{\text{eff}}} \right) - Y_0 \left(\frac{\rho}{r_{\text{eff}}} \right) \right] \chi_{j'}^m(\rho) = \frac{\beta^{2|m|}}{r_{\text{eff}}} \left[\frac{\Gamma(2|m|+3)}{\beta_j^{2|m|+3}} {}_3F_2 \left(|m|+1, |m|+\frac{3}{2}, |m|+2; \frac{3}{2}, \frac{3}{2}; -r_{\text{eff}}^{-2} \beta_{jj'}^{-2} \right) - 4^{|m|} r_{\text{eff}}^{2|m|+3} \cos(|m|\pi) \Gamma^2(|m|+1) {}_2F_1 \left(|m|+1, |m|+1; \frac{1}{2}; -r_{\text{eff}}^2 \beta_{jj'}^2 \right) \right], \quad (\text{A2b})$$

where ${}_pF_q(a_1, \dots, a_p; b_1, \dots, b_q; x)$ are generalized hypergeometric functions, and we have defined $\beta_{jj'} = \beta_j + \beta_{j'}$. Similarly, the RM overlap matrix elements are given by

$$S_{jj'}^m \equiv \int_0^\infty d\rho \rho \chi_j^{m*}(\rho) \chi_{j'}^m(\rho) = \beta^{2|m|} \int_0^\infty d\rho \rho^{2|m|+1} e^{-\beta_{jj'} \rho} = \beta^{2|m|} \frac{\Gamma(2|m|+2)}{\beta_{jj'}^{2|m|+2}}. \quad (\text{A3})$$

Appendix B: Matrix elements of the center-of-mass problem

The COM part of the Hamiltonian (1) with the trigonally-warped harmonic potential (13) can be written in cylindrical coordinates as

$$H_{\text{COM}} = -\frac{\hbar^2}{2M} \left(\frac{\partial^2}{\partial R^2} + \frac{1}{R} \frac{\partial}{\partial R} + \frac{1}{R^2} \frac{\partial^2}{\partial \Phi^2} \right) + \frac{M\omega^2}{2} R^2 + \delta V, \quad (\text{B1})$$

with the trigonal warping term

$$V = \frac{M\omega^2}{2} R^2 \cos(3\Phi + \varphi). \quad (\text{B2})$$

Using the basis states (14), which are eigenstates of the isotropic part of H_{COM} , we get the matrix elements

$$\langle \psi_{j', \mathcal{M}'} | H_{\text{COM}} | \psi_{j, \mathcal{M}} \rangle = \hbar \omega (j+1) \delta_{j', j} \delta_{\mathcal{M}', \mathcal{M}} - \delta \frac{\hbar \omega}{4} \frac{V_{j', j}^{\mathcal{M}', \mathcal{M}} \delta_{|\mathcal{M}-\mathcal{M}'|, 3}}{\sqrt{\left(\frac{j'-|\mathcal{M}'|}{2} + 1 \right)_{|\mathcal{M}'|} \left(\frac{j-|\mathcal{M}|}{2} + 1 \right)_{|\mathcal{M}|}}}, \quad (\text{B3})$$

where

$$V_{j', j}^{\mathcal{M}', \mathcal{M}} = \frac{2}{R_0^4} \int_0^\infty dR R^3 \left(\frac{R}{R_0} \right)^{|\mathcal{M}'|+|\mathcal{M}|} e^{-R^2/R_0^2} \times L_{(j'-|\mathcal{M}'|)/2}^{|\mathcal{M}'|} (R^2/R_0^2) L_{(j-|\mathcal{M}|)/2}^{|\mathcal{M}|} (R^2/R_0^2). \quad (\text{B4})$$

As discussed in the main text, the trigonal distortion of the potential leads to coupling between states with quantum numbers $\mathcal{M}' = \mathcal{M} \pm 3$, conserving angular momentum only modulo 3. To evaluate the radial part, we change variables to obtain⁵⁷

$$\begin{aligned}
V_{j',j}^{\mathcal{M}',\mathcal{M}} &= \int_0^\infty dx x^{\frac{|\mathcal{M}'|+|\mathcal{M}|}{2}+1} e^{-x} L_{\frac{j'-|\mathcal{M}'|}{2}}^{|\mathcal{M}'|}(x) L_{\frac{j-|\mathcal{M}|}{2}}^{|\mathcal{M}|}(x) \\
&= \frac{\Gamma\left(\frac{|\mathcal{M}'|+|\mathcal{M}|}{2}+2\right) (|\mathcal{M}'|+1) \frac{j'-|\mathcal{M}'|}{2} (|\mathcal{M}|+1) \frac{j-|\mathcal{M}|}{2}}{\left(\frac{j'-|\mathcal{M}'|}{2}\right)! \left(\frac{j-|\mathcal{M}|}{2}\right)!} \sum_{m=0}^{\frac{j'-|\mathcal{M}'|}{2}} \frac{\left(\frac{|\mathcal{M}'|-j'}{2}\right)_m \left(\frac{|\mathcal{M}'|+|\mathcal{M}|}{2}+2\right)_m}{(|\mathcal{M}'|+1)m!} \sum_{k=0}^{\frac{j-|\mathcal{M}|}{2}} \frac{\left(\frac{|\mathcal{M}|-j}{2}\right)_k \left(\frac{|\mathcal{M}'|+|\mathcal{M}|}{2}+2+m\right)_k}{(|\mathcal{M}|+1)k!}.
\end{aligned} \tag{B5}$$

Appendix C: Symmetry of the exciton wave function under C_3 rotations

Let $u_{\alpha,\tau,s,\mathbf{k}}(\mathbf{r})$ be the Bloch wave function of a $\tau\mathbf{K}$ -valley electron of band α and spin s , belonging to the symmetry group³² C_{3h} . This function transforms under C_3 rotations as $C_3 u_{\alpha,\tau,s,\mathbf{k}}(\mathbf{r}) = \phi_{\alpha,\tau} u_{\alpha,\tau,s,C_3\mathbf{k}}(\mathbf{r})$, where the eigenvalue $\phi_{\alpha,\tau}$ depends on the symmetry point in the lattice about which the rotation is performed [metal atom, chalcogen atom or hollow site; see Eq. (21)]. Accordingly, the creation operator for such an electron transforms as

$$C_3 c_{\alpha,\tau,s}^\dagger(\mathbf{k}) C_3^{-1} = \phi_{\alpha,\tau} c_{\alpha,\tau,s}^\dagger(C_3\mathbf{k}). \tag{C1}$$

From the field operator definition

$$\varphi_{\alpha,\tau,s}(\mathbf{r}) = \sum_{\mathbf{k}} \frac{e^{i(\tau\mathbf{K}+\mathbf{k})\cdot\mathbf{r}}}{\sqrt{S}} c_{\alpha,\tau,s}(\mathbf{k}), \tag{C2}$$

we find that

$$e^{-i\tau\mathbf{K}\cdot\mathbf{r}} C_3 \varphi_{\alpha,\tau,s}(\mathbf{r}) C_3^{-1} = \phi_{\alpha,\tau}^* e^{-i\tau\mathbf{K}\cdot C_3\mathbf{r}} \varphi_{\alpha,\tau,s}(C_3\mathbf{r}). \tag{C3}$$

Substituting (C3) into Eq. (18) gives

$$\begin{aligned}
C_3 |IX_{\tau',\tau}^{c',v;s}\rangle_{\tilde{\mathcal{M}},\ell}^{m,n} &= \phi_{c',\tau'} \phi_{v,\tau}^* \int d^2 r_e \int d^2 r_h e^{i\tau'\mathbf{K}'\cdot C_3\mathbf{r}_e - i\tau\mathbf{K}\cdot C_3\mathbf{r}_h} \\
&\times \Psi_{\tilde{\mathcal{M}},\ell}^{m,n}(\mathbf{r}_e, \mathbf{r}_h) \phi_{c',\tau',s}^\dagger(C_3\mathbf{r}_e) \phi_{v,\tau,s}(C_3\mathbf{r}_h) C_3 |\Omega\rangle \\
&= \phi_{c',\tau'} \phi_{v,\tau}^* \int d^2 \bar{r}_e \int d^2 \bar{r}_h e^{i\tau'\mathbf{K}'\cdot \bar{\mathbf{r}}_e - i\tau\mathbf{K}\cdot \bar{\mathbf{r}}_h} \\
&\times \Psi_{\tilde{\mathcal{M}},\ell}^{m,n}(C_3^{-1}\bar{\mathbf{r}}_e, C_3^{-1}\bar{\mathbf{r}}_h) \phi_{c',\tau',s}^\dagger(\bar{\mathbf{r}}_e) \phi_{v,\tau,s}(\bar{\mathbf{r}}_h) C_3 |\Omega\rangle,
\end{aligned} \tag{C4}$$

where $\bar{\mathbf{r}}_{e/h} = C_3\mathbf{r}_{e/h}$. From Eq. (19) we get $\Psi_{\tilde{\mathcal{M}},\ell}^{m,n}(C_3^{-1}\bar{\mathbf{r}}_e, C_3^{-1}\bar{\mathbf{r}}_h) = C_3 \Psi_{\tilde{\mathcal{M}},\ell}^{m,n}(\bar{\mathbf{r}}_e, \bar{\mathbf{r}}_h) = e^{-i\frac{2\pi}{3}(\tilde{\mathcal{M}}+m)} \Psi_{\tilde{\mathcal{M}},\ell}^{m,n}$. The many-body state $|\Omega\rangle$ must also be an eigenstate of the C_3 operator with some eigenvalue ϕ_Ω , resulting in Eq. (20).

Appendix D: Further moiré localized states

Figure 9 shows the COM wave functions of states $F_{\tilde{\mathcal{M}},\ell}$ for $(\tilde{\mathcal{M}} = 0, \ell = 3, 4, 5, 6, 7, 8)$ and $(\tilde{\mathcal{M}} = \pm 1, \ell = 3, 4, 5)$. States $F_{0,4}, F_{0,5}, F_{0,7}$ and $F_{0,8}$ belong to irrep A_1 of group C_{3v} , whereas $F_{0,3}, F_{0,6}$ belong to irrep A_2 . This can be inferred from the former's invariance under σ_v mirror operations, the latter's acquisition of a (-1) phase factor under the same, and all states' invariance under C_3 rotations. States $F_{\pm 1,3}, F_{\pm 1,4}$ and $F_{\pm 1,5}$ belong to the two dimensional irrep E . We have numerically verified their properties under C_3 rotations and σ_v mirror transformations.

* david.ruiz-tijerina@cnyun.unam.mx

- ¹ W. Yao, D. Xiao, and Q. Niu, Phys. Rev. B **77**, 235406 (2008).
- ² T. Cao, G. Wang, W. Han, H. Ye, C. Zhu, J. Shi, Q. Niu, P. Tan, E. Wang, B. Liu, and J. Feng, Nat. commun. **3**, 1 (2012).
- ³ K. F. Mak, K. He, J. Shan, and T. F. Heinz, Nat. nanotechnol. **7**, 494 (2012).
- ⁴ H. Zeng, J. Dai, W. Yao, D. Xiao, and X. Cui, Nat. nanotechnol. **7**, 490 (2012).
- ⁵ K. F. Mak, C. Lee, J. Hone, J. Shan, and T. F. Heinz, Phys. Rev. Lett. **105**, 136805 (2010).
- ⁶ A. Splendiani, L. Sun, Y. Zhang, T. Li, J. Kim, C.-Y. Chim, G. Galli, and F. Wang, Nano lett. **10**, 1271 (2010).
- ⁷ F. Ceballos, M. Z. Bellus, H.-Y. Chiu, and H. Zhao, ACS nano **8**, 12717 (2014).

- ⁸ J. Kunstmann, F. Mooshammer, P. Nagler, A. Chaves, F. Stein, N. Paradiso, G. Plechinger, C. Strunk, C. Schüller, G. Seifert, D. R. Reichman, and T. Korn, Nat. Phys. **14**, 801 (2018).
- ⁹ Y. Shimazaki, I. Schwartz, K. Watanabe, T. Taniguchi, M. Kroner, and A. Imamoğlu, Nature **580**, 472 (2020).
- ¹⁰ E. M. Alexeev, D. A. Ruiz-Tijerina, M. Danovich, M. J. Hamer, D. J. Terry, P. K. Nayak, S. Ahn, S. Pak, J. Lee, J. I. Sohn, *et al.*, Nature **567**, 81 (2019).
- ¹¹ W.-T. Hsu, B.-H. Lin, L.-S. Lu, M.-H. Lee, M.-W. Chu, L.-J. Li, W. Yao, W.-H. Chang, and C.-K. Shih, Sci. Adv. **5** (2019), 10.1126/sciadv.aax7407, <https://advances.sciencemag.org/content/5/12/eaax7407.full.pdf>.
- ¹² Y. Shimazaki, I. Schwartz, K. Watanabe, T. Taniguchi, M. Kroner, and A. Imamoğlu, Nature **580**, 472 (2020).

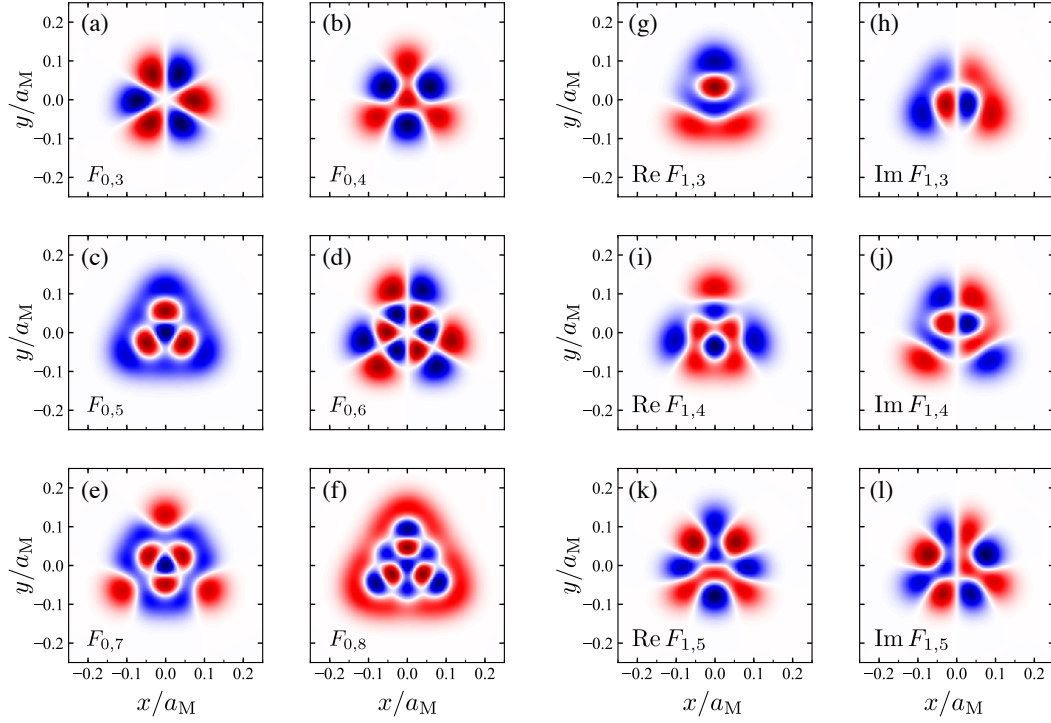


FIG. 9. Wavefunctions of moiré bound states in $R\text{-WSe}_2/\text{MoSe}_2$. As in Fig. 4, each function has been normalized to its maximum value for illustration purposes, and the color blue (red) indicates positive (negative) values, whereas white means a zero value. (a)-(f) $F_{0,\ell}$ for $3 \leq \ell \leq 8$. For $\ell = 4, 5, 7$ and 8 the functions are even under the mirror operations σ_v , σ'_v and σ''_v shown in Fig. 4(c), and belong to irrep A_1 of point group C_{3v} . By contrast, $F_{0,3}$ and $F_{0,6}$ belong to irrep A_2 , and are odd under the same mirror operations. (g)-(l) $F_{1,\ell}$ for $\ell = 3 \leq \ell \leq 5$, all of which belong to the two-dimensional irrep E . The corresponding wave functions from block $\bar{m} = -1$ can be obtained by complex conjugation.

- ¹³ M. Brotons-Gisbert, H. Baek, A. Molina-Sánchez, A. Campbell, E. Scerri, D. White, K. Watanabe, T. Taniguchi, C. Bonato, and B. D. Gerardot, *Nat. Mater.* **19**, 630 (2020).
- ¹⁴ M. Kuwabara, D. R. Clarke, and D. Smith, *Appl. Phys. Lett.* **56**, 2396 (1990).
- ¹⁵ H. Yu, G.-B. Liu, J. Tang, X. Xu, and W. Yao, *Science advances* **3**, e1701696 (2017).
- ¹⁶ F. Wu, T. Lovorn, and A. H. MacDonald, *Phys. Rev. Lett.* **118**, 147401 (2017).
- ¹⁷ F. Wu, T. Lovorn, and A. H. MacDonald, *Phys. Rev. B* **97**, 035306 (2018).
- ¹⁸ D. A. Ruiz-Tijerina and V. I. Fal'ko, *Phys. Rev. B* **99**, 125424 (2019).
- ¹⁹ C. Jin, E. C. Regan, A. Yan, M. I. B. Utama, D. Wang, S. Zhao, Y. Qin, S. Yang, Z. Zheng, S. Shi, *et al.*, *Nature* **567**, 76 (2019).
- ²⁰ L. Zhang, Z. Zhang, F. Wu, D. Wang, R. Gogna, S. Hou, K. Watanabe, T. Taniguchi, K. Kulkarni, T. Kuo, S. R. Forrest, and H. Deng, (2019), arXiv:1911.10069 [cond-mat.mes-hall].
- ²¹ K. L. Seyler, P. Rivera, H. Yu, N. P. Wilson, E. L. Ray, D. G. Mandrus, J. Yan, W. Yao, and X. Xu, *Nature* **567**, 66 (2019).
- ²² K. Tran, G. Moody, F. Wu, X. Lu, J. Choi, K. Kim, A. Rai, D. A. Sanchez, J. Quan, A. Singh, *et al.*, *Nature* **567**, 71 (2019).
- ²³ M. Brotons-Gisbert, H. Baek, A. Molina-Sánchez, A. Campbell, E. Scerri, D. White, K. Watanabe, T. Taniguchi, C. Bonato, and B. D. Gerardot, *Nat. Mater.* **19**, 630 (2020).
- ²⁴ H. Yu, Y. Wang, Q. Tong, X. Xu, and W. Yao, *Phys. Rev. Lett.* **115**, 187002 (2015).
- ²⁵ M. Danovich, D. A. Ruiz-Tijerina, R. J. Hunt, M. Szyniszewski, N. D. Drummond, and V. I. Fal'ko, *Phys. Rev. B* **97**, 195452 (2018).
- ²⁶ L. V. Keldysh, *J. Exp. Theor. Phys.* **29**, 658 (1979).
- ²⁷ J. A. Wilson and A. Yoffe, *Advances in Physics* **18**, 193 (1969).
- ²⁸ A. Al-Hilli and B. Evans, *Journal of Crystal Growth* **15**, 93 (1972).
- ²⁹ D. Yang and R. Frindt, *Journal of Physics and Chemistry of Solids* **57**, 1113 (1996).
- ³⁰ R. Pisoni, A. Kormányos, M. Brooks, Z. Lei, P. Back, M. Eich, H. Overweg, Y. Lee, P. Rickhaus, K. Watanabe, T. Taniguchi, A. Imamoglu, G. Burkard, T. Ihn, and K. Ensslin, *Phys. Rev. Lett.* **121**, 247701 (2018).
- ³¹ S. Larentis, H. C. P. Movva, B. Fallahazad, K. Kim, A. Behroozi, T. Taniguchi, K. Watanabe, S. K. Banerjee, and E. Tutuc, *Phys. Rev. B* **97**, 201407 (2018).
- ³² A. Kormányos, G. Burkard, M. Gmitra, J. Fabian, V. Zólyomi, N. D. Drummond, and V. Fal'ko, *2D Materials* **2**, 022001 (2015).
- ³³ M. V. Gustafsson, M. Yankowitz, C. Forsythe, D. Rhodes, K. Watanabe, T. Taniguchi, J. Hone, X. Zhu, and C. R. Dean, *Nature materials* **17**, 411 (2018).
- ³⁴ P. V. Nguyen, N. C. Teutsch, N. P. Wilson, J. Kahn, X. Xia, A. J. Graham, V. Kandyba, A. Giampietri, A. Barinov, G. C. Constantinescu, N. Yeung, N. D. M. Hine, X. Xu, D. H. Cobden, and N. R. Wilson, *Nature* **572**, 220 (2019).
- ³⁵ B. Fallahazad, H. C. P. Movva, K. Kim, S. Larentis, T. Taniguchi, K. Watanabe, S. K. Banerjee, and E. Tutuc, *Phys. Rev. Lett.* **116**, 086601 (2016).
- ³⁶ E. Mostaani, M. Szyniszewski, C. H. Price, R. Maezono, M. Danovich, R. J. Hunt, N. D. Drummond, and V. I. Fal'ko, *Phys. Rev. B* **96**, 075431 (2017).
- ³⁷ K. Xu, Y. Xu, H. Zhang, B. Peng, H. Shao, G. Ni, J. Li, M. Yao, H. Lu, H. Zhu, *et al.*, *Physical Chemistry Chemical Physics* **20**, 30351 (2018).
- ³⁸ T. C. Berkelbach, M. S. Hybertsen, and D. R. Reichman, *Phys. Rev. B* **88**, 045318 (2013).
- ³⁹ A. Chernikov, T. C. Berkelbach, H. M. Hill, A. Rigosi, Y. Li, O. B. Aslan, D. R. Reichman, M. S. Hybertsen, and T. F. Heinz, *Phys. Rev. Lett.* **113**, 076802 (2014).
- ⁴⁰ F. J. Asturias and S. R. Aragón, *American Journal of Physics* **53**, 893 (1985), <https://doi.org/10.1119/1.14360>.
- ⁴¹ X. L. Yang, S. H. Guo, F. T. Chan, K. W. Wong, and W. Y. Ching, *Phys. Rev. A* **43**, 1186 (1991).
- ⁴² J. J. Griffin and J. A. Wheeler, *Phys. Rev.* **108**, 311 (1957).
- ⁴³ A. Baldereschi and N. O. Lipari, *Phys. Rev. B* **8**, 2697 (1973).
- ⁴⁴ F. Mireles and S. E. Ulloa, *Phys. Rev. B* **58**, 3879 (1998).
- ⁴⁵ F. Mireles and S. E. Ulloa, *Applied Physics Letters* **74**, 248 (1999), <https://doi.org/10.1063/1.123270>.
- ⁴⁶ Z. Ye, T. Cao, K. O'Brien, H. Zhu, X. Yin, Y. Wang, S. G. Louie, and X. Zhang, *Nature* **513**, 214 (2014).
- ⁴⁷ M. Van der Donck and F. M. Peeters, *Phys. Rev. B* **99**, 115439 (2019).
- ⁴⁸ As mentioned in Sec. II, short-ranged interlayer interactions are overestimated by the Keldysh formula (3). This results in overestimation of the binding energies of the lowest energy states, particularly 1s.
- ⁴⁹ C. Gong, H. Zhang, W. Wang, L. Colombo, R. M. Wallace, and K. Cho, *Applied Physics Letters* **103**, 053513 (2013).
- ⁵⁰ W.-K. Li and S. Blinder, *Journal of mathematical physics* **26**, 2784 (1985).
- ⁵¹ G. Wang, C. Robert, M. M. Glazov, F. Cadiz, E. Courtade, T. Amand, D. Lagarde, T. Taniguchi, K. Watanabe, B. Urbaszek, and X. Marie, *Phys. Rev. Lett.* **119**, 047401 (2017).
- ⁵² H. Yu, G.-B. Liu, and W. Yao, *2D Mater.* **5**, 035021 (2018).
- ⁵³ G.-B. Liu, D. Xiao, Y. Yao, X. Xu, and W. Yao, *Chemical Society Reviews* **44**, 2643 (2015).
- ⁵⁴ Q. Tong, H. Yu, Q. Zhu, Y. Wang, X. Xu, and W. Yao, *Nature Physics* **13**, 356 (2017).
- ⁵⁵ Notable exceptions to this rule are ¹⁰MoSe₂/WS₂, and possibly ¹⁸MoTe₂/MoSe₂, where strong interlayer hybridization of carriers has been predicted and/or observed experimentally. Nonetheless, these heterostructures are chalcogen mismatched and possess short moiré periodicities, making them poor candidates for exciton localization by moiré potentials.
- ⁵⁶ Y. Wang, Z. Wang, W. Yao, G.-B. Liu, and H. Yu, *Phys. Rev. B* **95**, 115429 (2017).
- ⁵⁷ G. E. Andrews, R. Askey, and R. Roy, *Special functions*, Vol. 71 (Cambridge university press, 1999).